Quantitative experimental monitoring of molecular diffusion in clay with positron emission tomography

Johannes Kulenkampff, Abdelhamid Zakhnini, Marion Gründig, Johanna Lippman-Pipke

Institute of Resource Ecology, Helmholtz-Zentrum Dresden-Rossendorf, Germany

5 *Correspondence to*: J. Kulenkampff (j.kulenkampff@hzdr.de)

Abstract. Clay plays a prominent role as barrier material in the geosphere. The small particle sizes cause extremely small pore sizes and induce low permeability and high sorption capacity. Transport of dissolved species by molecular diffusion is less sensitive to the pore size. Heterogeneous structures on centimetre scale could cause heterogeneous effects, like preferential transport zones, which are difficult to assess. Laboratory measurements with diffusion cells yield limited

10 information on heterogeneity, and pore space imaging methods have to consider scale effects. We established positron emission tomography (PET); applying a high-resolution PET-scanner, as spatially resolved quantitative method for direct laboratory observation of the diffusion process of a PET-tracer on the prominent scale of 1–100 mm. Although PET is rather insensitive to bulk effects, quantification required significant improvements of the image reconstruction procedure with respect to Compton scatter and attenuation. The experiments were conducted with ^{22}Na and ^{124}I over periods of 100,

15 respectively 25 days. From the images we derived trustable anisotropic diffusion coefficients and, in addition, we identified indications for preferential transport zones. We thus demonstrated the unique potential of the PET imaging modality for geoscientific process monitoring under conditions where other methods fail, taking advantage of the extremely high detection sensitivity that is specific to radiotracer applications.

20
Keywords: Process tomography, positron emission tomography, PET, diffusion, clay, anisotropy, heterogeneity, tracer

1 Introduction

Natural clay typically has a heterogeneous composition and a spatially variant anisotropic structure. Due to grain sizes of the clay fraction in the micrometre range, pore sizes are extremely small. This effectively inhibits advective flow and causes high internal surface area, forming natural geological barriers. However, natural sediments have to be considered as

5 heterogeneous material. In particular, in Opalinus clay (OPA) we not only observe heterogeneity on the micrometre scale (Keller et al., 2011), but also laminations and concretions on the millimetre-scale (Fig. 1) which potentially provide either preferential diffusion pathways or specific sorption sites, respectively. Therefore, standard millimetre-sized samples in diffusion cell experiments cannot be considered as homogeneous. As smallest possible size of the representative elementary volume (REV) we consider the size of standard drill cores, because their size is just above the largest observed

10 heterogeneities. It still is an open question, if a REV exists beyond which the material may be considered as homogeneous, or if analogical heterogeneities exist on larger scales.

This question is relevant for a number of safety cases, because clay layers are generally considered as geological barrier for safe enclosure of hazardous substances. Preferential zones with higher diffusion rates generally are less tortuous, which also means a smaller effective internal surface area. Therefore, these zones delimit the barrier function both by increased

15 diffusion rate and decreased retention, which have to be considered as worst case scenario.

Determination of these heterogeneous parameters with common diffusion-cell experiments is laborious and requires a large number of studies in order to match these delimiting zones (Van Loon et al., 2004). Also, the detailed characterization on the pore space with multiscale x-ray imaging is particularly intricate, because a hierarchy of structures over many orders should be considered, from surface characteristics on the molecular scale to fine-layering on the centimetre scale.

20 As another option we introduced a quantitative visualization of the diffusing species (Kulenkampff et al., 2015). We applied positron emission tomography (PET) as totally selective and most sensitive imaging method for positron-emitting radionuclides. PET responds to the spatial distribution of positron decay events which are detected as coinciding antiparallel photons with energy of 511 keV. The mass attenuation is at a minimum in this energy range which allows the reconstruction of the spatial distribution of positron decay events in rock samples up to diameters of 100 mm.

25 However, strong effects of Compton scattering and attenuation of the 511-keV-radiation have to be considered. Earlier, we identified these effects as considerable issue with regard to quantification of the tracer concentration (Zakhnini et al., 2013); the resulting images rather had to be considered as qualitative. Scattering and some deficiencies of the reconstruction procedure had caused blurring and imaging artefacts, and the fit of a conceptual diffusion model to these data had produced unexplainable high diffusion coefficients (Kulenkampff et al., 2012). These issues could be solved to a large extent with a

30 proper scatter correction procedure which is outlined in this article, and we are now able to make quantitative use.

2 Materials and methods

2.1 Measurements

A horizontal drill core (diameter = 100 mm, length = 80 mm) of OPA from Mont Terri was cast in epoxy resin (Fig. 1). The sample is not considered to be undisturbed, because fracturing due to the stress release and drying during storage is probable.

5 This situation is representative rather for the excavation damage zone than for undisturbed host rock in the far field.

Perpendicular to the bedding, an axillar blind hole (diameter = 5 mm, length = 50 mm) was drilled into the core and filled with synthetic OPA pore water (Pearson et al., 2003). After an equilibration period, which included observations with ^{124}I-labelled OPA-water, equilibration, the hole was filled with synthetic OPA-water, now labelled with ^{22}Na with an initial activity of 18 MBq. Then it was closed with a screw, establishing a physically sealed source. The sample was stored at 20°

10 C. Beginning daily, with increasing time lag, a sequence of 20 PET images was recorded over a period of 143 days until the tracer was roughly equally distributed throughout the core. The length of these frames was 40 min.

We applied a ClearPET scanner manufactured by Raytest (Sempere Roldan et al., 2007). This is a high-resolution PET scanner designated for biomedical research on small animals that was originally developed by the Crystal Clear Collaboration (http://crystalclear.web.cern.ch/crystalclear/Default.html). In contrast to clinical PET-scanners with a spatial

15 resolution of 3–5 mm, this class of scanners reaches the fundamental physical resolution limit of about 1 mm, depending on material density; the voxel dimensions are 1.15 mm, accordingly. This high resolution is achieved at the expense of technically unavoidable gaps between the detector crystals, which cause an inhomogeneous sensitivity matrix. This loss of homogeneity is mitigated by rotating the gantry.

2.2 Image reconstruction

20 The raw PET data are projections of the spatial tracer distribution. These projections correspond to lines of response (LOR) connecting the detection points of the antiparallel photon pair that was transmitted by the annihilating positron–electron pair. These photons undergo attenuation and Compton scattering, which both are controlled by the mass attenuation coefficient which depends directly on material density. Because the density of geomaterials is considerably higher than biological tissue, we have to consider corrections for these effects more thoroughly than in common biomedical or clinical PET applications.

25 Details of the method are reported in Kulenkampff et al. (2016). Here, we focus on the implementation and calibration of the scatter correction procedure, which showed significant impact on the experimental results.

In (Zakhnini et al., 2013) we applied a Monte Carlo (MC) simulation procedure for determining the impact of scattered events and for developing a tentative correction procedure. This procedure is extremely demanding with respect to computing resources and takes at least several hours for each image. The MC simulations were conducted with the open-

30 source simulation platform GATE (Jan et al., 2004). Input parameters are scanner geometry, sample geometry ("phantom"), material parameters, and source parameters. The source parameters include geometry, activity, and the significant contributions of the decay spectrum of the particular nuclides. In addition to the experimentally applied nuclides ^{18}F, ^{22}Na,

and ^{124}I we also considered ^{48}V, ^{58}Co, ^{64}Cu, ^{86}Y, and ^{132}La, as possible tracer for studying geochemical effects. These isotopes are either commercially available or can be produced with our in-house cyclotron "Cyclone® 18/9" (IBA Molecular, Belgium) (Mansel, 2015; Mansel et al., 2014).

In contrast to the real physical world, MC provides a means to study the history of all recorded events, from the positron

5   decay to the detection. This includes a comprehensive parametrisation of scattering, taking into account the magnitude and origins of scatter, and the distributions of energy, the order of scatter, and scattering angles. We also studied the effects of different potential PET nuclides, because different initial positron energies and additional gamma radiation have different impact on the recorded data. We have to distinguish

- N_{tot}: total number of coincidences,

10 - N_{rand}: number of random coincidences (coincidences that are not from the identical positron decay event),

- N_{sc}: number of scattered coincidences,

- N_{trus}: number of true (non-random) unscattered coincidences,

- N_{fals}: "false" coincidences, coinciding spurious gamma radiation.

The global MC-results with respect to the nuclides are depicted in Fig. 2. It should be noted, that all parameters are functions

15 of both PET-nuclide and matrix material. Comparison of the data sets with a ^{22}Na-source in clay and in water shows that the portion of coincidences which are not affected by material effects (N_{trus}/N_{tot}) is considerably higher in water (52.3%) than in clay (31.8%). This is also reflected by the scatter fraction

$$SF = \frac{N_{sc}}{N_{tot}}.$$

The high scatter fraction, in combination with attenuation up to 80%, is the reason for annoying blurring effect. The

20 deviations of the LORs from the straight connection between source and detector positions are in the order of centimetres. This contradicts the presupposition of the reconstruction algorithm and causes considerable circular imaging artefacts.

The mean order of scattering (number of Compton interactions per registered coincidence) is more than 3, therefore the premises for single-scatter modelling as basis for a scatter correction procedure are not satisfied, and the applicability has to be verified. However, the mean scatter angle is in the range of small-angle scattering (below 10°) with maximum values

25 around 20°.

In contrast to the preceding paper (Zakhnini et al., 2013) we abandoned the version 1.4 of STIR, which was the originally supplied image reconstruction library and switched to the recent version 3.0 (Thielemans et al., 2012). As before, we applied corrections for random coincidences and attenuation. The normalization process was improved according to (Weber et al., 2006) in order better to consider the effect of void bins in the projections caused by the gaps between the detectors.

30 The recent version of the reconstruction software, since STIR 2.1 (Tsoumpas et al., 2004), supplies a simpler and faster analytical scatter modelling method than MC which is based on Watson et al. (1996). It is an approximation of the deviations of the coincidences along each LOR according to the Klein-Nishina equation for Compton-scatter. Scatter correction of

multiple time frames becomes practicable with an optimized procedure which typically requires 30 min on a standard CPU for each frame.

This single scatter simulation algorithm (SSS) does not account for multiple scattered events and scatter from sources and scatter points outside the FOV. It requires as input data the distribution of mass attenuation coefficients, as measure of the scatter cross section, and an estimate of the source, usually an uncorrected image. Multiple scattering is approximately considered by scaling of the scatter estimate and by iterative application of the procedure (Polycarpou et al., 2011). The customary calibration of the SSS-correction is then conducted by fitting the simulated scatter events to the measured events outside the region of the source distribution. Because of the large number of void bins in this marginal region of the FOV of the ClearPET-scanner, this method is unreliable. We therefore take advantage from the results of the MC-simulations, with which we are able to determine the scatter fraction SF quantitatively, and vary the scaling factor of the SSS iteratively until the scatter fraction from the MC-simulation is matched (Fig. 3). In order to avoid over-compensation of the scatter, we assume a target value which is 10% lower than the simulated scatter fraction, because the simulation includes additional sources of scatter (e.g. in the detector crystals and in material outside the FOV).

In order to calibrate the scatter correction model, we thus need an estimate of the scatter fraction which either is the result of one single MC-simulation of a rough model, or we consider a standard calibration factor of 5 for our scanner as conservative estimation.

The outcome of the SSS is in general accordance with the result of the MC-simulation: We reconstructed images from the MC-data sets

- all true coincidences *tot* (no scatter correction)
- unscattered *unsc* (reference image)
- only scattered coincidences *sc*
- SSS-corrected with scaling factor 5 and 10.

In Fig. 4 we computed the circular mean values of the axial projections of these images, yielding the intensity vs. the radial distance from the central line source in clay. The impact of scattering becomes clear at distances above 5 mm, and without scatter correction the intensity becomes dominated by scatter (*tot* and *sc*). The SSS-correction scaled with a factor 10, which is the intersection point in Fig. 3, yields data below the line of the reference image which therefore are overcorrected. With a factor 5 they are undercorrected, and scatter effects are dominating in regions far from the source. We assume that this is the region of high scattering angles and multiple scatter which is not considered by the SSS-algorithm. It should be noted that the ordinate of Fig. 4 is scaled logarithmically, and that these deviations are more than two orders below the source intensity. We recommend slight undercorrection to avoid the creation of additional void bins.

3 Results

As example, we report the measurements on one sample (BLT 137/3): Beginning daily, with increasing time lag, we produced a sequence of 20 PET-images over a period of 150 days until the tracer was roughly equally distributed over the core (Fig. 5) (t = 0, 3, 6, 10, 13, 16, 20, 22, 27, 31, 35, 41, 48, 55, 69, 93, 112, 127, 143, 161 days). Because of the large

5 amplitude range the images were scaled frame-wise. Figure 6 shows the evolution of the maximum value, which is the reference, and the 90% and 99.9%-quantile. Figure 7 shows slices in the direction of the major anisotropy axes. A gas bubble becomes visible, which at frame 1 had moved from its initial position at the bottom of the hole. The maximum projection in vertical direction is plotted as height-map at the bottom of each frame. It indicates that the diffusing tracer reaches the sample surface after 31 days at frame 10. Then, the tracer distribution homogenises over the sample; therefore, the quantiles

10 stabilize (Fig. 6) and the anisotropy of the distribution decreases until frame 18, which shows almost homogeneous tracer distribution.

Figure 8 is an enlargement of the maximum projection of frame 9, after one month. The shape of this distribution appears as roughly 10 mm thick rectangular block, rather than as an anisotropy ellipsoid, notwithstanding remaining indications for circular artefacts. This type of shape could be interpreted as an indication for diffusion along fine layering, rather than

15 homogenous transversal anisotropic behaviour. However, these findings should be assured by additional investigations (e.g. µCT, radiography and analysis of thin sections, as well as model simulations) and after further improvement of image quality.

Prior to the investigations with ^{22}Na we tested ^{124}I as PET-tracer (Fig. 9). In principle, its decay time (4.176 d) allows observations periods up to 1 month, sufficient for parameter derivations according to the procedure outlined below.

20 However, the images are noisy, because of other "parasitic" γ-radiation ("false coincidences"), and the decreasing count rate causes an increasing error with time. Therefore, application of ^{124}I merely is a qualitative test method, rather than suited for quantitative estimations.

4 Discussion

In the past we experienced problems with the correction methods that had been supplied with the scanner, because these had

25 been designed for material with low attenuation and scatter. Attenuation model and scatter correction had been derived from measured data, a procedure that increased the noise level unacceptably. Instead, we implemented a method which bases upon attenuation and scatter modelling. Their establishment is simple, because of the plain geometry of the samples. The expedience of the STIR-SSS for scatter modelling has been proven with MC-simulations, and calibration factors have been found.

30 With these corrections we could reconstruct clear and sharpened images which retained a minimum scatter component. Features became visible that had been covered by blurring effects and new levels of detail were identified. A gas bubble became clearly distinguishable. The extension of the tracer cloud, which had been apparently wide-spread due to scatter

effects, became localized and bounded. An optimum fit of an updated finite-element model now yields anisotropic diffusion coefficients in the range of literature results ($D_{xx} = D_{zz} = 10.2\text{e-}11 \text{ m}^2 \text{ s}^{-1}$ and $D_{yy} = 2.2\text{e-}11 \text{ m}^2 \text{ s}^{-1}$) (Lippmann-Pipke et al., 2016). We therefore conclude that the only transport process is molecular diffusion. This is in contrast to our first hypothesis, which was misled by inadequate consideration of the scatter effect, where we presumed that suction into partially saturated

5   zones of the sample caused accelerated spreading of the tracer.

We fitted anisotropy ellipses to the axial projections of the data in order to determine direct experimental anisotropy parameters and to estimate the propagation velocity of the tracer front. The position of this front was defined as the location of the FWHM-line (full width half maximum). From Fig. 11 we read a propagation velocity of 0.5 mm d^{-1} and 2 mm d^{-1} for the smallest and the largest axis, respectively. This is in accordance with results that were calculated from literature values

10   by Lippmann-Pipke et al. (2016).

We also computed the ratio b/a of these major axes of the FWHM for all frames, as shown in Fig. 12. Apparently, this anisotropy ratio is not constant, but increases steadily with time until the tracer propagation front reaches the sample surface after 31 days. This initial increase of anisotropy could be caused by preferential diffusion continuing along a rather linear pathway, in contrast to homogeneous anisotropic behaviour. The subsequent decrease of b/a is caused by increasing

15   equilibration of the tracer concentration over the complete sample.

Figure 8 may explain this situation. Here, the amplitude distribution appears as roughly rectangular region with thickness of about 2 cm, rather than as a lineament. Therefore the anisotropic behaviour could be caused by a thin layer with elevated diffusion properties.

It is not yet possible to compare these findings with structural images before the tracer activity decayed. This will be topic of

20   a subsequent study.

As they are controlled by the topology of the pathways, such heterogeneous effects are only observable on sufficiently large samples. These effects should be taken into account for transport simulations on the field scale, because preferential diffusion zones could accelerate diffusional transport not only by increased directional transport. Zones which are not effectively taking part in the diffusional transport process are inefficient with respect to sorption as well. Therefore, the

25   retention parameters are decreasing simultaneously. This could further amplify the acceleration of the diffusional propagation.

5 Conclusions

We established PET as tomographic method for diffusion imaging. We take advantage from the extreme sensitive detection of decay radiation which is a beneficial characteristic of radiometric methods in general. PET is applicable as non-

30   destructive method for quantitative determination of the spatiotemporal tracer distribution in complete drill cores. From these data, integral anisotropic diffusion coefficients can be computed which are comparable to the results of a large set of single one-dimensional diffusion-cell experiments on small specimen. Beyond that, it is presently the only quantitative method

which enables to study effects of heterogeneities on the centimetre scale, in particular preferential diffusion zones. Such zones could have significant impact on the diffusional propagation of chemical species on the field scale.

Acknowledgements. The authors thank the Federal Ministry for Economic Affairs and Energy for financial support of this
5 study (grant no. 02E10971) and the Project Management Agency Karlsruhe (Water Technology and Waste Management Division) for administration.

References

Jan, S., Santin, G., Strul, D., Staelens, S., Assie, K., Autret, D., Avner, S., Barbier, R., Bardies, M., Bloomfield, P. M., Brasse, D., Breton, V., Bruyndonckx, P., Buvat, I., Chatziioannou, A. F., Choi, Y., Chung, Y. H., Comtat, C., Donnarieix, D., Ferrer, L., Glick, S. J., Groiselle, C. J., Guez, D., Honore, P. F., Kerhoas-Cavata, S., Kirov, A. S., Kohli, V., Koole, M., Krieguer, M., Laan, D. J. v. d., Lamare, F., 15 Largeron, G., Lartizien, C., Lazaro, D., Maas, M. C., Maigne, L., Mayet, F., Melot, F., Merheb, C., Pennacchio, E., Perez, J., Pietrzyk, U., Rannou, F. R., Rey, M., Schaart, D. R., Schmidtlein, C. R., Simon, L., Song, T. Y., Vieira, J. M., Visvikis, D., Walle, R. V. d., Wieers, E., and Morel, C.: GATE: a simulation toolkit for PET and SPECT, Physics in Medicine and Biology, 49, 4543-4561, 2004.
Keller, L. M., Holzer, L., Wepf, R., and Gasser, P.: 3D geometry and topology of pore pathways in 20 Opalinus clay: Implications for mass transport, Applied Clay Science, 52, 85-95, 10.1016/j.clay.2011.02.003, 2011.
Kulenkampff, J., Gründig, M., Schikora, J., Zakhnini, A., and Lippmann-Pipke, J.: Long-term spatiotemporal monitoring of diffusion processes in Opalinus drill cores with GeoPET and parameterization with Comsol Multiphysics, 5th International Meeting on Clays in Natural and 25 Engineered Barriers for Radioactive Waste Confinement, Montpellier, France, 22.-25.10.2012, 2012.
Kulenkampff, J., Gründig, M., Zakhnini, A., Gerasch, R., and Lippmann-Pipke, J.: Process tomography of diffusion, using PET, to evaluate anisotropy and heterogeneity, Clay Minerals, 50, 369-375, 10.1180/claymin.2015.050.3.09, 2015.
Kulenkampff, J., Gründig, M., Zakhnini, A., and Lippman-Pipke, J.: Geoscientific process monitoring 30 with positron emission tomography (GeoPET), Solid Earth, this issue, 2016.
Lippmann-Pipke, J., Gerasch, R., Schikora, J., and Kulenkampff, J.: Benchmarking PET for geoscientific applications: 3D quantitative diffusion coefficient estimation in clay rock, Computational Geosciences, submitted, 2016.
Mansel, A., Gruhne, S., Franke, K., and Fischer, S.: Production of 85Sr at a 18 MeV-cyclotron and 35 purification for geochemical investigations, Applied Radiation and Isotopes, 92, 22-24, 10.1016/j.apradiso.2014.06.001, 2014.
Mansel, A. F., K.: Production of no-carrier-added ^{135}La at an 18 MeV cyclotron and its purification for investigations at a concentration range down to 10^{-15} mol / L, Radiochimica Acta, 103, 759-763, 10.1515/ract-2015-2427, 2015.

Pearson, F. J., Arcos, D., Bath, A., Boisson, J.-Y., Fernández, A. M., Gäbler, H.-E., Gaucher, E., Gautschi, A., Griffault, L., Hernán, P., and Waber, H. N.: Mont Terri Project – Geochemistry of Water in the Opalinus Clay Formation at the Mont Terri Rock Laboratory, Eidgenössisches Departement für Umwelt, Verkehr, Energie und Kommunikation, Bern, 321, 2003.

5   Polycarpou, I., Thielemans, K., Manjeshwar, R., Aguiar, P., Marsden, P. K., and Tsoumpas, C.: Comparative evaluation of scatter correction in 3D PET using different scatter-level approximations, Annals of nuclear medicine, 25, 643-649, 10.1007/s12149-011-0514-y, 2011.

Sempere Roldan, P., Chereul, E., Dietzel, O., Magnier, L., Pautrot, C., Rbah, L., Sappey-Marinier, D., Wagner, A., Zimmer, L., Janier, M., Tarazona, V., and Dietzel, G.: Raytest ClearPET(TM), a new
10 generation small animal PET scanner, Nuclear Instruments and Methods in Physics Research Section A: Accelerators, Spectrometers, Detectors and Associated Equipment, 571, 498-501, 2007.

Tsoumpas, C., Aguiar, P., Nikita, K. S., Ros, D., and Thielemans, K.: Evaluation of the single scatter simulation algorithm implemented in the STIR library, IEEE Nuclear Science Symposium and Medical Imaging Conference, 16-22 Oct., 2004.

15 Van Loon, L. R., Soler, J. M., Müller, W., and Bradbury, M. H.: Anisotropic Diffusion in Layered Argillaceous Rocks: A Case Study with Opalinus Clay, Environmental Science & Technology, 38, 5721-5728, 10.1021/es049937g, 2004.

Watson, C. C., Newport, D., and Casey, M. E.: A Single Scatter Simulation Technique for Scatter Correction in 3D PET, in: Three-Dimensional Image Reconstruction in Radiology and Nuclear
20 Medicine, edited by: Grangeat, P., and Amans, J.-L., Computational Imaging and Vision, Springer Netherlands, 255-268, 1996.

Zakhnini, A., Kulenkampff, J., Sauerzapf, S., Pietrzyk, U., and Lippmann-Pipke, J.: Monte Carlo simulations of GeoPET experiments: 3D images of tracer distributions (18F, 124I and 58Co) in Opalinus Clay, anhydrite and quartz, Computers & Geosciences, 57, 183-196,
25 10.1016/cageo.2013.03.023, 2013.

30
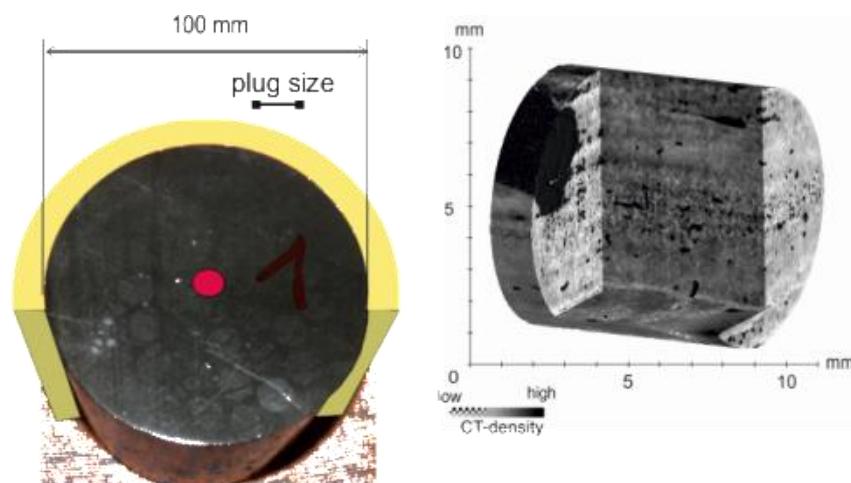
Figures:

5   **Figure 1: Left: OPA drill core before embedding in resin ("plug size" refers to the dimensions of the µCT-image). Right: µCT-image of a mini-plug from the same formation (recorded at the Federal Institute for Material Research and Testing BAM, Berlin). Figure taken from Kulenkampff et al. (2015).**

	F-18	Na-22	V-48	Co-58	Cu-64	Y-86	I-124	La-132		Na-22 W
Ntrus/Ntot	34.7%	31.8%	32.4%	43.6%	38.4%	27.9%	38.7%	29.7%		52.3%
Nrand/Ntot	11.4%	18.7%	25.4%	14.1%	2.1%	39.1%	11.2%	38.5%		14.1%
Nfals/Ntot	0.0%	12.5%	39.3%	42.4%	0.2%	56.8%	24.7%	62.0%		7.6%
Nsc/Ntot	53.8%	49.5%	42.2%	42.3%	59.5%	32.9%	50.1%	31.7%		33.6%
MeanOrder	3.37	3.42	3.55	3.57	3.38	3.61	3.46	3.61		3.11
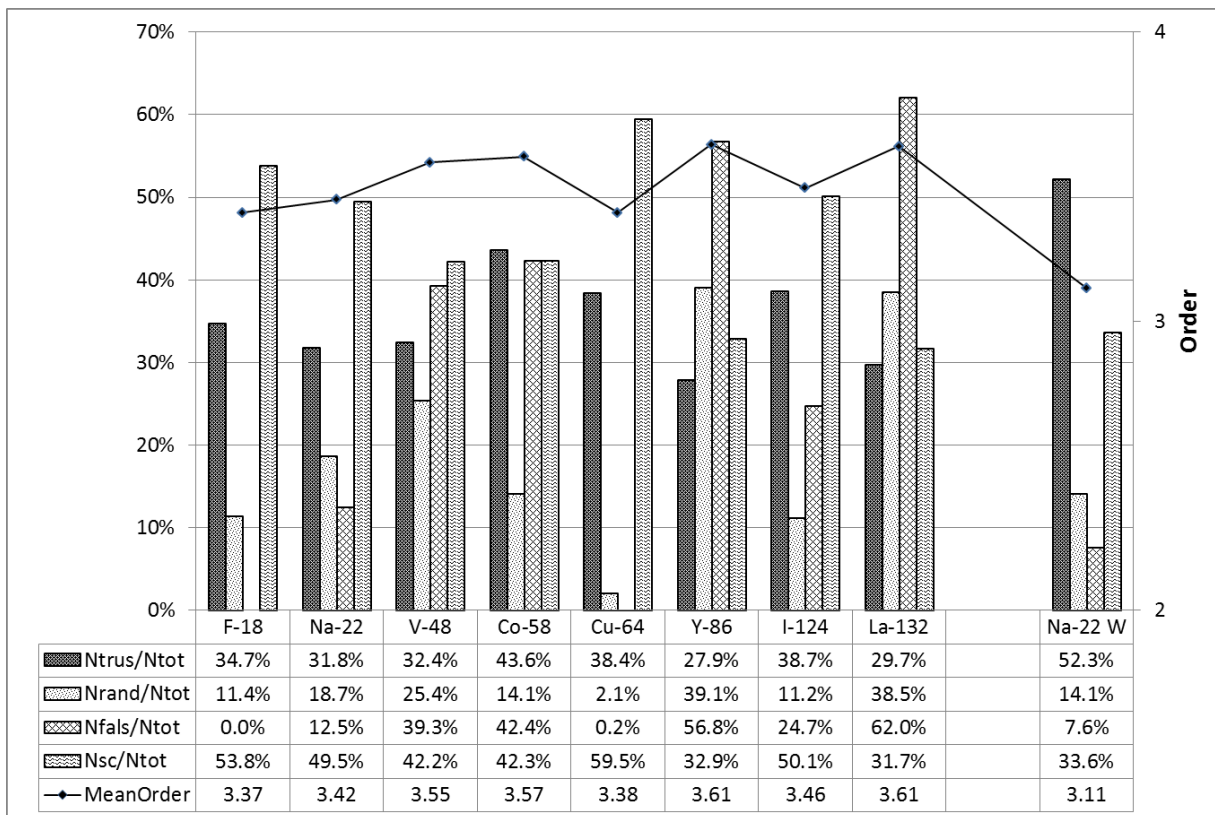
Figure 2: Global result of the MC-simulations. Left: Line source in Opalinus clay, filled with ^{18}F, ^{22}Na, ^{48}V, ^{58}Co, ^{64}Cu, ^{86}Y, ^{124}I, and ^{132}La. Right: ^{22}Na - line source in water.
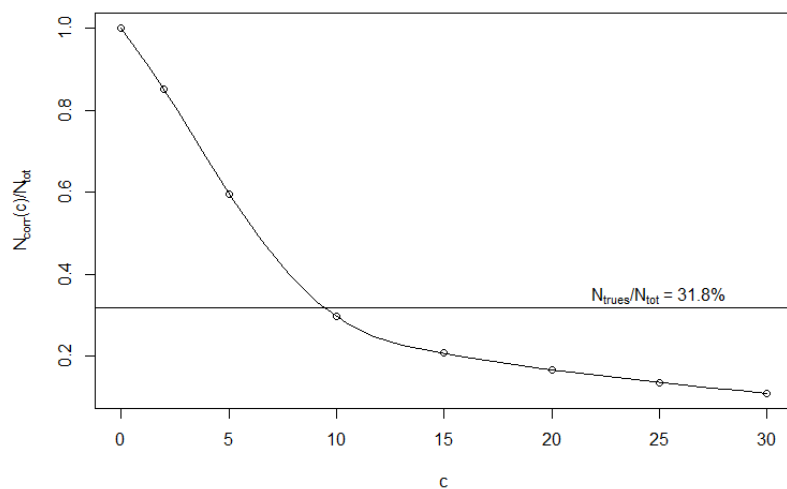
Figure 3: Relative number of scatter corrected coincidences $N_{corr}(c)/N_{tot}$ versus the scatter calibration factor c. The horizontal reference line was derived from the MC-simulation (Fig. 2, Na-22).
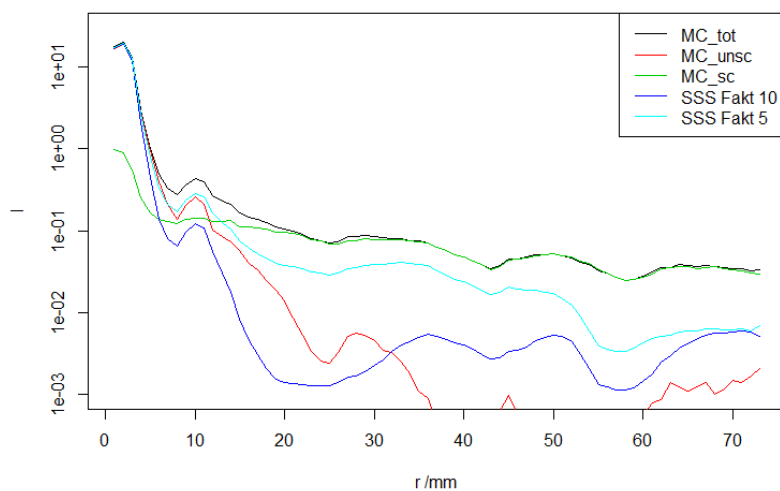
Figure 4: Intensity I vs. radial distance r from the central line source of images, in dependence of the type of scatter correction (MC_tot: total true coincidences *tot*, MC_unsc: only unscattered coincidences *unsc*, MC_sc: only scattered coincidences *sc*, SSS_Fakt_10/SSS_Fakt_5: all true coincidences (*tot*) with SSS-correction and scaling factor 10 and 5, respectively).
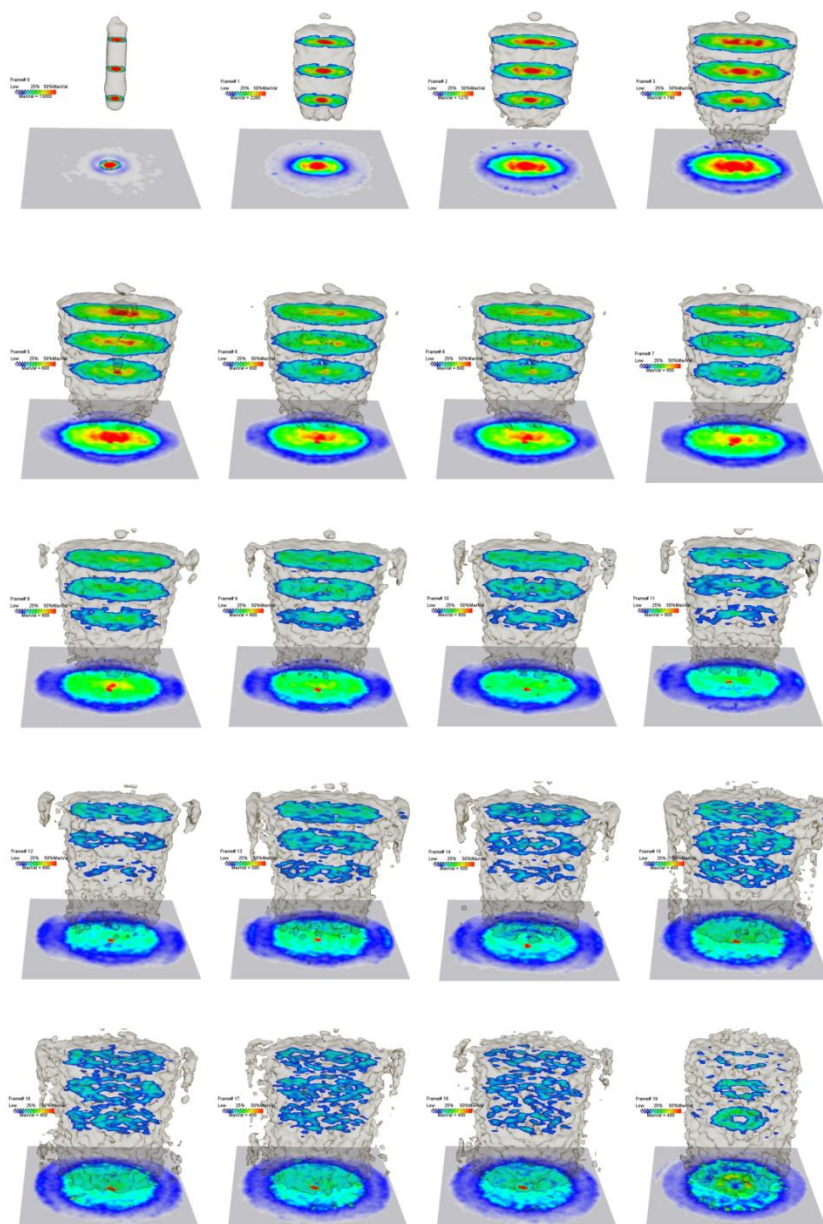
Figure 5: 20 PET-frames of ^{22}Na-diffusion in an OPA-drill core (diameter: 100 mm, length 80 mm). Each frame is depicted as iso-surface of the one-tenth maximum value (grey), three horizontal slices through the source region, and the axial (vertical) maximum projection at the bottom. The colour ranges are scaled frame-wise; the maximum value of the colour range is half maximum total amplitude (corresponding amplitude distribution see Fig. 6).
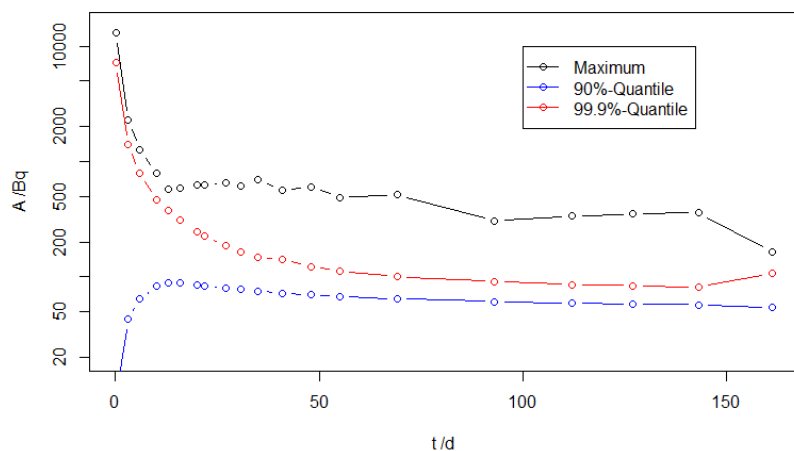
Figure 6: Maximum, 99.9%- and 90%-quantiles of the amplitude vs. frame time of Fig.5. The colour scale in Fig. 5 refers to the maximum value.
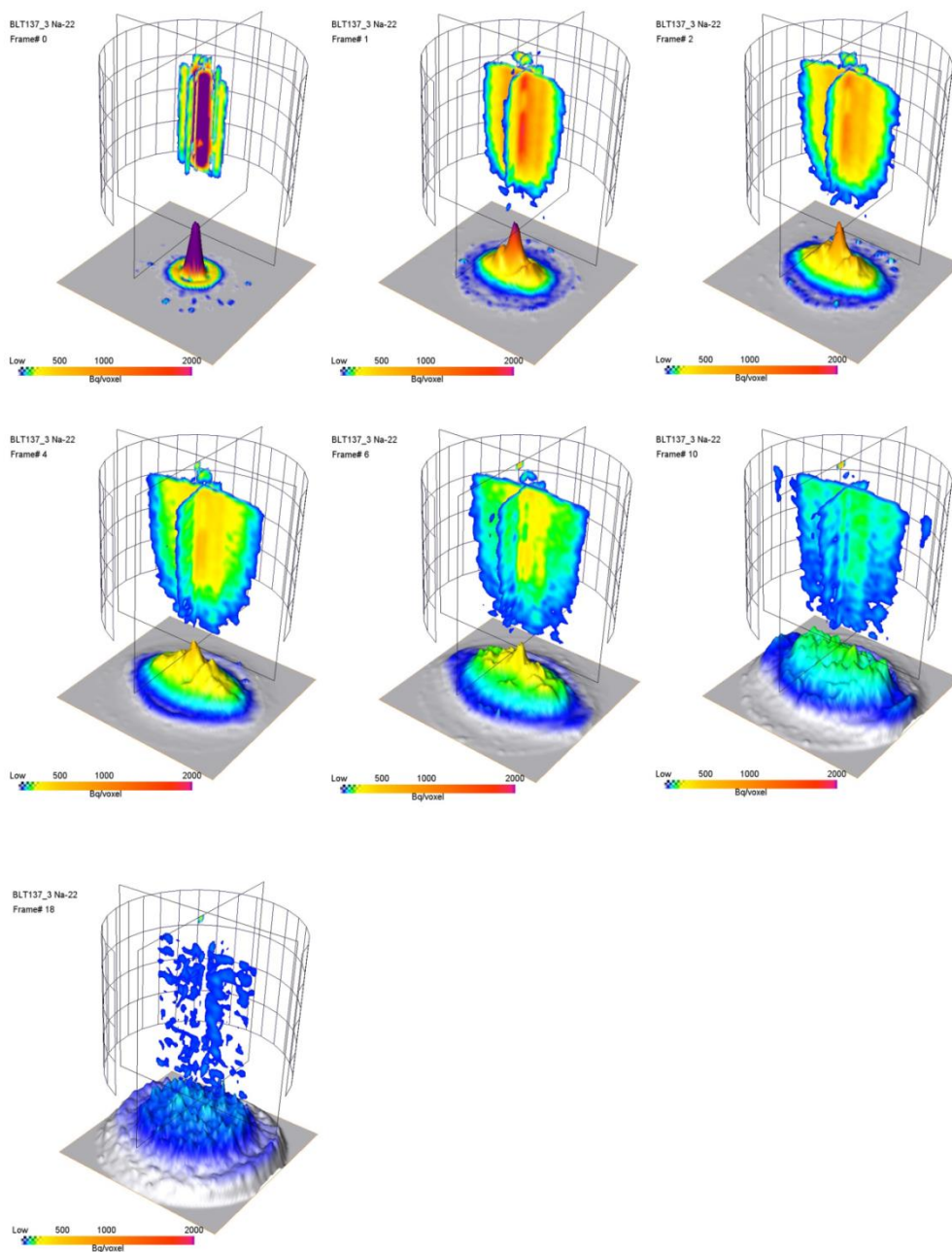
Figure 7: Vertical slices and axial projection of the first seven frames of Fig. 5, with uniform colour scale. After frame 7 the tracer arrived at the cylinder surface.

BLT137_3 Na-22
Frame# 9
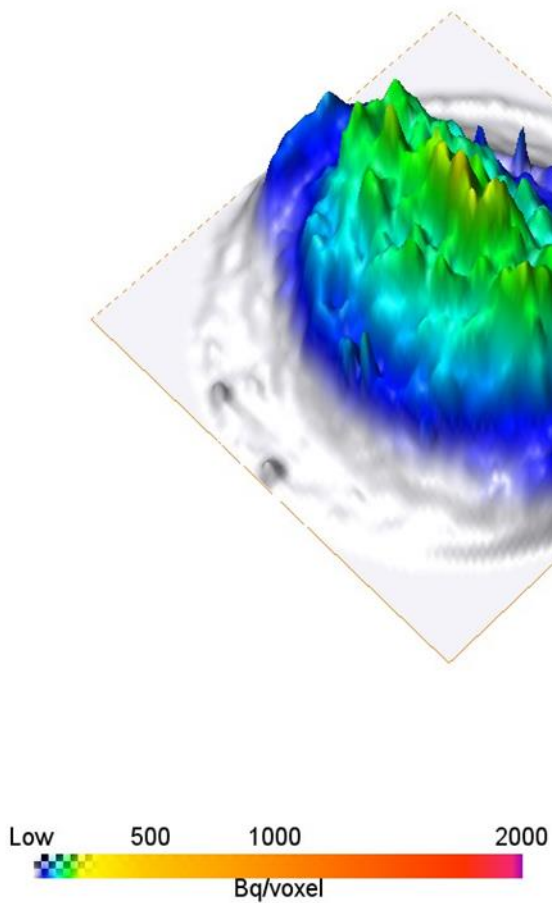
Figure 8: Axial maximum projection of frame 9 (27 days), when the tracer distribution reached the circumference.
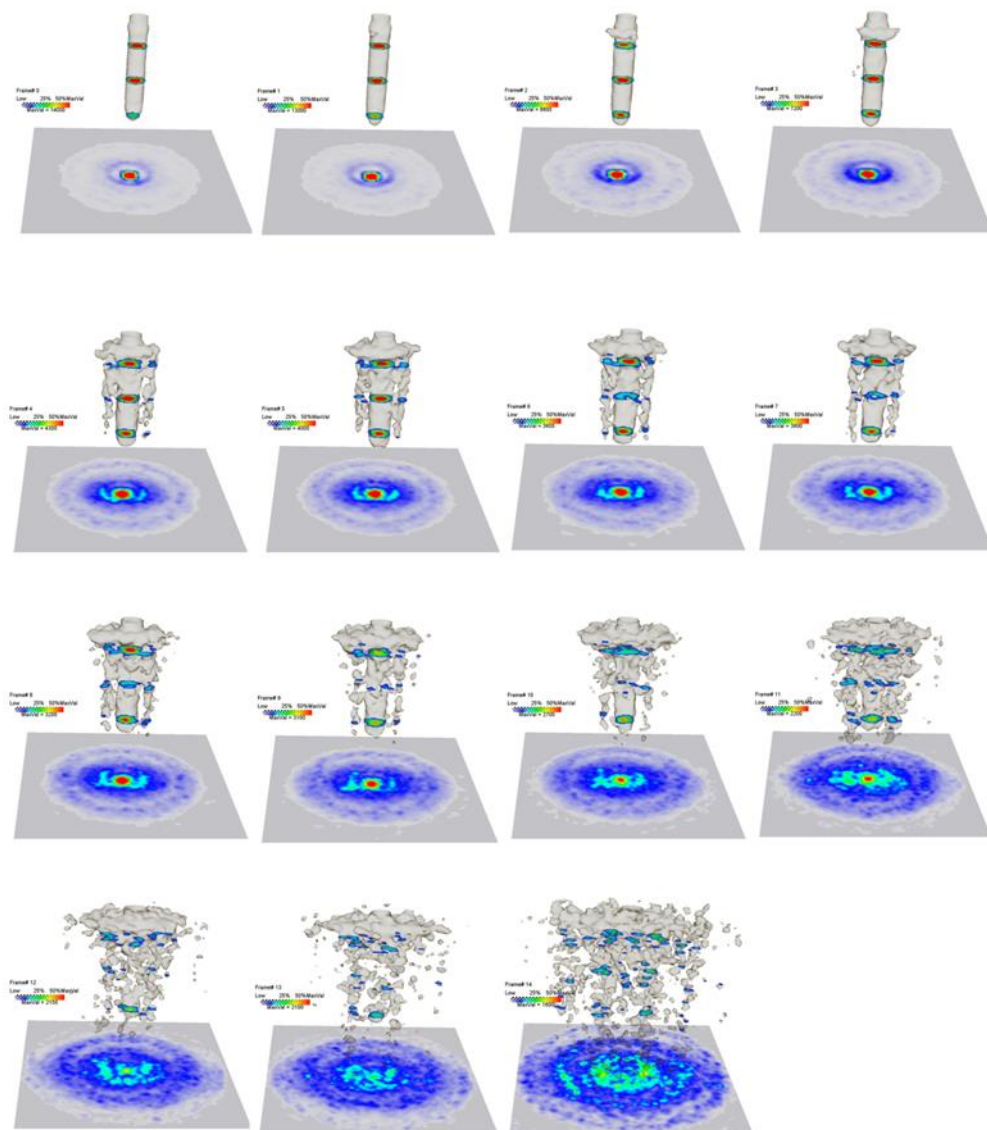
Figure 9: 15 PET-frames of ^{123}I-diffusion in an OPA-drill core (diameter: 100 mm, length 80 mm). Each frame is depicted as iso-surface of the one-tenth maximum value (grey), three horizontal slices through the source region, and the axial (vertical) maximum projection at the bottom. The colour ranges are scaled frame-wise; the maximum value of the colour range is half maximum total amplitude (corresponding amplitude distribution see Fig. 10).
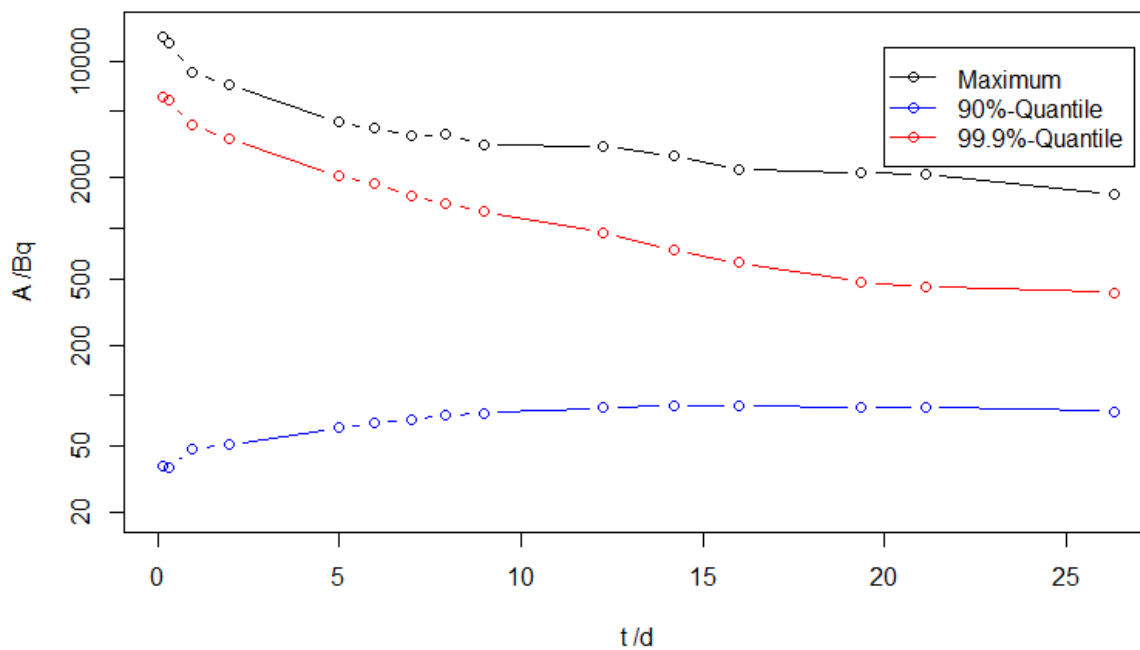
Figure 10: Maximum, 99.9%- and 90%-quantiles of the amplitude of Figure 9 vs. frame time of Fig. 9. The colour scale in Fig. 9 refers to the maximum value.
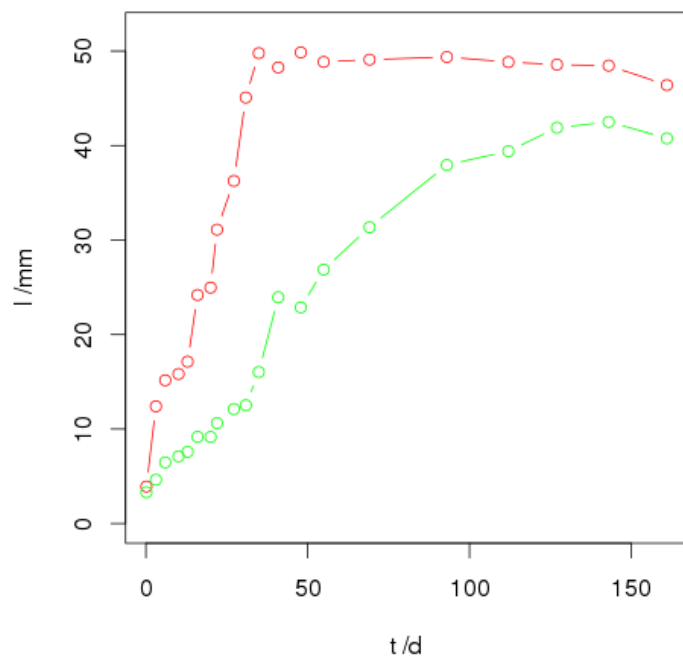
Figure 11: Lengths of the major axes of the FWHM vs. frame time (red: fast axis, green: slow axis) of the [22]Na-experiment.
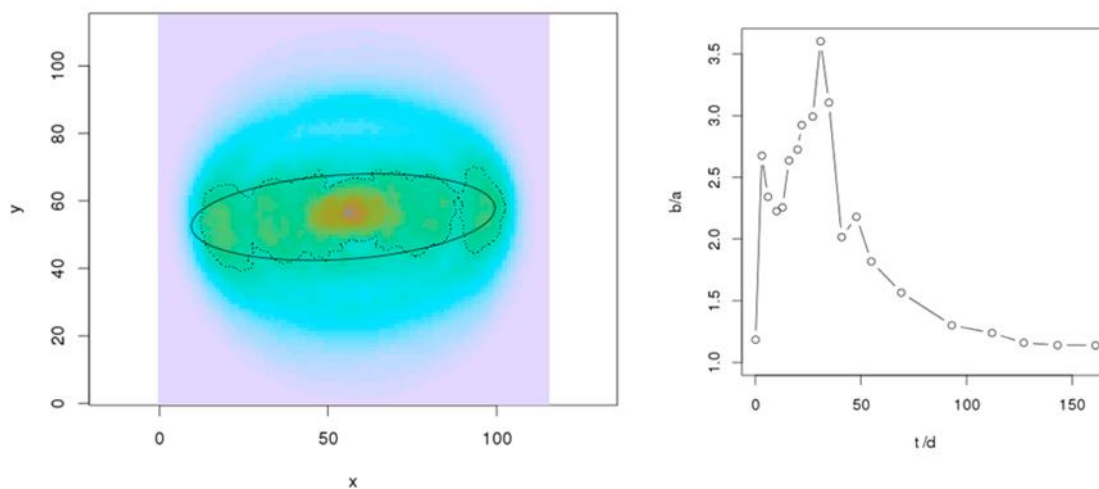
5   **Figure 12: Left: Axial projection of the activity distribution with elliptical fit of the FWHM-curve of the ninth frame after 27 days (see Fig. 8), right: temporal evolution of the ratio of the major anisotropy axis.**